Kshitij Kumar Yadav[1]
Department of Civil and Environmental Engineering,
University of Massachusetts,
Amherst, MA 01003
e-mail: kkyadav@umass.edu

Nicholas L. Cuccia
School of Engineering and Applied Sciences,
Harvard University,
Cambridge, MA 02138
e-mail: cuccia@g.harvard.edu

Emmanuel Virot
School of Engineering and Applied Sciences,
Harvard University,
Cambridge, MA 02138
e-mail: sgerasimidis@umass.edu

Shmuel M. Rubinstein
School of Engineering and Applied Sciences,
Harvard University,
Cambridge, MA 02138
e-mail: emmanuel.virot@polytechnique.edu

Simos Gerasimidis
Department of Civil and Environmental Engineering,
University of Massachusetts,
Amherst, MA 01003
e-mail: shmuel@seas.harvard.edu

A Nondestructive Technique for the Evaluation of Thin Cylindrical Shells' Axial Buckling Capacity

The axial buckling capacity of a thin cylindrical shell depends on the shape and the size of the imperfections that are present in it. Therefore, the prediction of the shells buckling capacity is difficult, expensive, and time consuming, if not impossible, because the prediction requires a priori knowledge about the imperfections. As a result, thin cylindrical shells are designed conservatively using the knockdown factor approach that accommodates the uncertainties associated with the imperfections that are present in the shells; almost all the design codes follow this approach explicitly or implicitly. A novel procedure is proposed for the accurate prediction of the axial buckling capacity of thin cylindrical shells without measuring the imperfections and is based on the probing of the axially loaded shells. Computational and experimental implementation of the procedure yields accurate results when the probing is done in location of highest imperfection amplitude. However, the procedure overpredicts the capacity when the probing is done away from that point. This study demonstrates the crucial role played by the probing location and shows that the prediction of imperfect cylinders is possible if the probing is done at the proper location.
[DOI: 10.1115/1.4049806]

Keywords: computational mechanics, elasticity, failure criteria, structures

1 Introduction

Thin cylindrical shells are widely used due to their structural efficiency, ease of construction, and appeal to aesthetics. However, this comes at a cost—they are highly sensitive to imperfections. The presence of even a small imperfection [1–19] can reduce a shells' axial buckling capacity significantly. Therefore, the presence of imperfections induces an element of uncertainty. The reduction in the shells' axial buckling capacity depends on the shape and the size of each imperfection, as well as their topological arrangement. Thus, one requires an a priori knowledge about the imperfections to make accurate failure predictions. Measuring all the imperfections, however, is a difficult, expensive, and time consuming, thus making the prediction of a shells' capacity nontrivial, if not impossible.

Nearly all cylindrical structures couple a high degree of imperfection sensitivity with unknown underlying imperfections. Thin cylindrical shells are thus designed conservatively using the knockdown factor approach; almost all the design codes follow this approach explicitly or implicitly, e.g., NASA [20] and Eurocode [21]. Through these design rules, we have learnt to live with the problem that has long been an obstacle for the efficient use of thin shells. Recently, the quest for high-fidelity estimates of the buckling capacity has regained significant attention due to the renewed interest in space-flight and in thin soft material [22–29]. Indeed, a promising new framework based on the probing of axially compressed cylinders has emerged for the evaluation of the buckling capacity of thin cylindrical shells without complete knowledge of the shell's underlying imperfections: the stability landscape [7,30–46]. However, this framework is still in the infant state, and many issues have to be resolved, e.g., the role of probing location, the influence of the imperfection's size and shape, and the impact of the interaction among imperfections.

Here, we explore some of these issues by combining numerical analysis with experiments as a stepping stone toward the development of a nondestructive technique for the evaluation of thin cylindrical shells buckling capacity. We address the issues of extracting information from probe force–displacement curves and using this information to predict the capacity. In addition, we investigate the role of probing location, imperfections amplitude, and background imperfections on the accuracy of the prediction.

First, we propose an algorithm to predict the buckling capacity of thin shells; this algorithm is based on the feedback of probe force–displacement curves of axially loaded shells. Then, the proposed algorithm is computationally implemented on thin perfect and imperfect shells ($R/t \approx 286$), and we find that it provides accurate results. Next, we experimentally predict the capacity of close-to-perfect shells and imperfect shells. To create the imperfect shells, a novel experimental technique is developed for a systematic introduction of geometrical imperfections of a set scale. The experimental implementation of the algorithm gives an accurate prediction for the high imperfection amplitudes, while for low imperfection amplitudes, experiments fail to predict the capacities. In all our experimental and computational studies, we probe in the center of the preexisting dimple imperfection of the shells. The location of the imperfection is crucial information that may not be available for real structures. To study the impact of the location of probing relative to the imperfection, we probe away from the imperfection in the circumferential and axial direction. This reveals that the location of probing affects the ability of the proposed method to predict the buckling capacity of the shells. We find that the probing is inferring only local information, and thus, the prediction becomes less and less accurate as the probing is

[1]Corresponding author.

Contributed by the Applied Mechanics Division of ASME for publication in the Journal of Applied Mechanics. Manuscript received October 28, 2020; final manuscript received January 10, 2021; published online February 4, 2021. Assoc. Editor: Pedro Reis.

Table 1 Dimensions and material properties of aluminum mini Coke cans (7.5 fl oz) used for the computational model

E (GPa)	R (mm)	ν	t (μm)	L (mm)
68.95	28.6	0.3	100	107

moving away from the imperfection. Overall, this study demonstrates many aspects of the probing of axially loaded thin cylindrical shells: (1) probing can be used to predict the buckling capacity of shells containing a dimple imperfection, (2) the probing location plays a crucial role in the accuracy of the prediction, and (3) a framework can be developed for nondestructive experiments to predict the buckling capacity of thin shells.

2 Description of the Procedure and Its Application on a Perfect Cylindrical Shell

The proposed procedure takes advantage of the stability landscape of axially loaded shells. The method consists of three steps: (1) shells are put under axial load F_a, (2) these axially loaded shells are probed in radial direction at the location of a preexisting imperfection, and (3) the peak probe force $F_p^{\max}$ and the corresponding axial load F_a are recorded and are used to predict the axial capacity. There are two constraints on the axial load F_a: (1) F_a is less than the axial capacity of the cylinders and (2) when axially compressed cylinders are probed, there exist a peak in probe force–displacement curves. The constraint on the probing is that the probe displacement $D_p < 5t$, where t is the thickness of cylinders. The second constraint is based on the phenomenological observations from hundreds of computations and experiments that a peak in the probing force will appear for probe displacements $D_p < 5t$. Beyond that probe displacement, a peak in the probing force is not likely to appear. In addition, probing beyond $5t$ could also induce undesired plastic deformations, which have not yet been quantified either computationally or experimentally. The three steps of the procedure are iterated with increasing axial load F_a till the predicted axial capacity F_{pre} converges. The convergence criterion is $|F_{pre} - F_a| < 0.1F_{pre}$, where F_{pre} is the predicted capacity and F_a is the largest axial load. We are using this convergence criterion because it gives accurate predictions, any other criteria could be used if that gives a good prediction.

Initially, the cylinder is compressed under axial load $F_a = 0.5\kappa P_c$, where κ is the knockdown factor of the cylinder, which is an empirical finding based the experiments performed in late sixties [20], and P_c is the classical axial buckling capacity of the perfect cylinder. For a cylindrical shell with radius R, thickness t, Young's modulus E, and Poisson's ratio ν, the values of P_c and κ [20] are represented as follows:

$$P_c = \frac{2\pi E t^2}{\sqrt{3(1-\nu^2)}} \tag{1}$$

$$\kappa = 1 - 0.901\left(1 - \exp\left(\frac{\sqrt{R/t}}{16}\right)\right) \tag{2}$$

This initial value of F_a is less than half of the expected capacity κP_c (assuming the cylinder is imperfect) of the cylinder, and thus, the first constraint on F_a is fulfilled. To enforce the second constraint on F_a, we probe the cylinder that is under axial load $F_a = 0.5\kappa P_c$. The probing is done at the location, where the amplitude of imperfection is maximum, with the constraint $D_p < 5t$. If $F_p^{\max}$ exists in the probe force, then F_a and $F_p^{\max}$ will be $F_{a,1}$ and $F_{p,1}^{\max}$, the first data set for the axial force and peak probe force that is used for the capacity prediction. If $F_p^{\max}$ does not exist in the probe force then F_a is increased by 10%, and the cylinder is probed again at the same location. This iteration is continued till we find an identifiable peak $F_p^{\max}$ in probe force.

In the proposed procedure, a minimum of five pairs of $\{F^a; F_p^{\max}\}$ are needed for the capacity prediction. Once we have the first data set $\{F_{a,1}; F_{p,1}^{\max}\}$, we can find the next four data sets $\{F_{a,2}; F_{p,2}^{\max}\}$, $\{F_{a,3}; F_{p,3}^{\max}\}$, $\{F_{a,4}; F_{p,4}^{\max}\}$, and $\{F_{a,5}; F_{p,5}^{\max}\}$ following Eq. (3).

$$F_{a,i} = F_{a,i-1} + 0.05F_{a,1} \tag{3}$$

$F_{p,i}^{\max}$ is the peak probe force of the cylinder that is axially loaded under $F_{a,i}$. After having the five data sets, we predict the capacity of the cylinder by quadratic curve fitting of these data sets. The predicted capacity F_{pre} is the value of Y-axis where the quadratic curve intercepts it assuming F_a corresponds to Y-axis, and $F_p^{\max}$ corresponds to X-axis. If the convergence criterion $|F_{pre} - F^a| < 0.1F_{pre}$ is satisfied, F_{pre} will be the capacity of the cylinder. Otherwise, a new data set $\{F_{a,i+1}, F_{p,i+1}^{\max}\}$ is added following Eq. (4).

$$F_{a,i+1} = F_{a,i} + cF_{pre} \tag{4}$$

$F_{p,i+1}^{\max}$ is the peak probe force corresponds to $F_{a,i+1}$, and c is a constant whose value depends on $|F_{pre} - F_a|$. The values of c are 0.25, 0.20, 0.15, 0.10, and 0.05 for $|F_{pre} - F_a| > 0.50F_{pre}$, $|F_{pre} - F_a| > 0.40F_{pre}$, $|F_{pre} - F_a| > 0.30F_{pre}$, $|F_{pre} - F_a| > 0.20F_{pre}$,

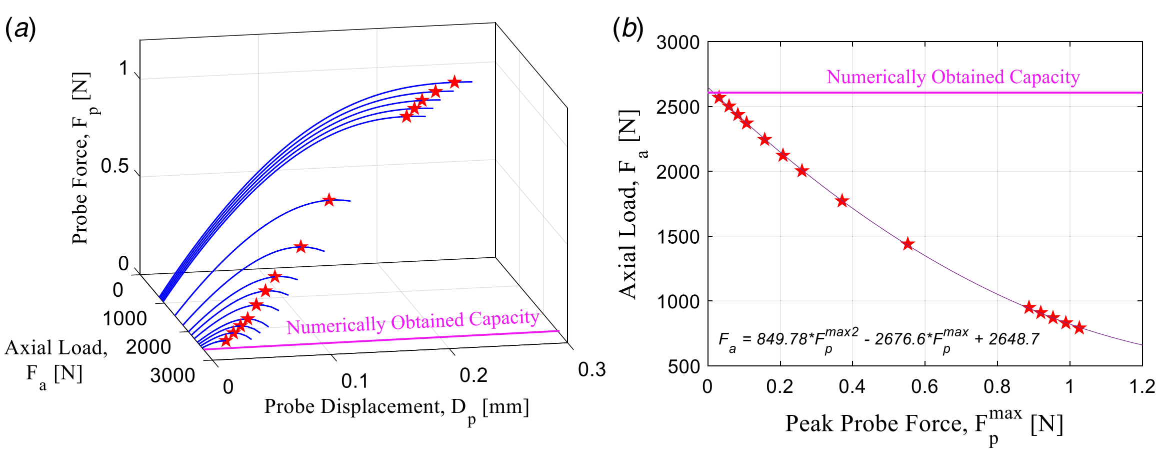

Fig. 1 **(a) Stability landscape, which is obtained by implementing the proposed procedure numerically, shown in the three-dimensional phase space of axial load F_a, probe displacement D_p, and probe force F_p. (b) The axial load F_a versus peak probe force $F_p^{\max}$ data along with its quadratic regression curve. The predicted capacity F_{pre}, where the quadratic curve intercepts Y-axis, of the cylinder is 2648.7 N, whereas the numerically obtained capacity of the cylinder F_{num} is 2584.7 N and is shown by the horizontal line.**

and $|F_{pre} - F_a| > 0.10F_{pre}$, respectively. $|F_{pre} - F_a| < 0.10F_{pre}$ is the convergence criteria; the iteration stops at this point, and F_{pre} is the predicted capacity of the cylinder.

To illustrate the proposed procedure, we apply this computationally using finite element analysis (FEA) package ABAQUS [47] on a perfect cylinder that models mini Coke cans (7.5 fl oz), made of aluminum. The dimensions and material properties of the Coke can are presented in Table 1. The advantage of using cans is that they are easily available for our experiments. The modeling technique follows the one presented by Haynie et al. [48]. The mesh for the models was created by user-written codes using $S4R$ elements with an element size of 0.91 mm, about $0.54\sqrt{Rt}$, in both axial and circumferential directions. The boundary conditions at the ends of the cylinder are applied using the same procedure as by Haynie et al. [48] with rigid links, which connect the central node to the nodes at the ends of the cylinder. Further, we simplified our modeling assuming the cross sections of cans are circular throughout the length, which is a slight deviation from the physical cans. This does not affect our analysis as here the purpose is the evaluation of the proposed procedure and not to emulate the experiments exactly. For a perfect cylinder, probing can be done anywhere, as there is no imperfection. However, we probe in the middle section of the cylinder to avoid any effects of boundaries. For step 1 of the procedure, geometrically nonlinear static analysis is used to put the cylinder under prescribed axial load, and for step 2, the arc-length-based Riks method [49] is used to probe the cylinder in the radial direction.

Figure 1(*a*) shows the stability landscape—a two-dimensional surface in a three-dimensional phase space of axial load F_a, probe displacement D_p, and probe force F_p— of the cylinder. This force landscape is obtained by implementing the proposed procedure. The prediction converges after 14 iterations, and thus, 14 probe force–displacement curves are shown. In Fig. 1(*b*), the axial load F_a versus peak probe force $F_p^{\max}$ is shown along with their quadratic regression curve (polynomial fit of order 2). The predicted capacity the cylinder, where the quadratic curve intercepts the Y axis, F_{pre} is 2648.7 N, whereas the numerically obtained capacity (using FEA) of the cylinder F_{num} is 2584.7 N and shown in Fig. 1(*b*) by the horizontal line.

The percentage difference between the F_{pre} and F_{num} is 2.5% ($|F_{num} - F_{pre}|/F_{num} \times 100$); this shows that the proposed procedure is predicting the capacity of a perfect cylinder accurately. However, the real challenge of the procedure is when it is used for imperfect cylinders. This is the subject of Sec. 3.

3 Application of the Procedure on Imperfect Cylindrical Shells

To apply the proposed procedure on imperfect cylinders, we induce a local dimple imperfection in the middle of the perfect cylinder. The dimple imperfection is modeled as a two-dimensional normal distribution function following Gerasimidis et al. [50] and Yadav and Gerasimidis [18]. The mathematical description of the dimple imperfection is given as follows:

$$w = -\delta e^{-(x-x_0/L_1)^2} e^{-(\theta-\theta_0/\theta_1)^2} \tag{5}$$

where w represents the deviation from the original position in the radial direction, δ is the amplitude of the imperfection, x and θ are the axial and circumferential coordinates (x_0 and θ_0, respectively) are the center of the dimple whose values are chosen such that the dimple is located in the middle section of the cylinder. L_1 and θ_1 are the parameters that dictate the length (in the axial direction) and the width (in the circumferential direction) of the dimple. In this study, the value of L_1 and θ_1 are 0.55λ and $0.55\lambda/R$ [18], where λ is the half-wavelength of classical axisymmetric buckling mode of the cylindrical shell under axial load, and its value is given by Eq. (6) [51]. This dimple is introduced in the perfect cylinder whose dimensions are given in Table 1. Figure 2 shows the

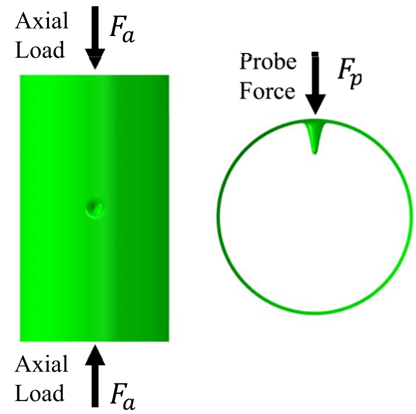

Fig. 2 Imperfect cylinder, and its cross section in the middle. The imperfection is modeled as a dimple in the shape of a two-dimensional normal distribution density function [18,50]. The dimple is located in the middle section, and the probing is done in the center of the dimple. The amplitude of the dimple is scaled up so that it is visible in the image.

dimple-like imperfect cylinder along with axial load F_a and probe force F_p that is applied radially inward in the middle of the dimple.

$$\lambda = \pi \sqrt{\frac{Rt}{\sqrt{12(1-\nu^2)}}} \tag{6}$$

We apply the proposed procedure computationally using FEA package ABAQUS [47] on the imperfect cylinder. For step 2 of the procedure, the probing is done in the middle of the dimple. The output of the procedure for imperfection amplitude $\delta = 0.1t$ is shown in Fig. 3. Fig. 3(*a*) shows the stability landscape, and Fig. 3(*b*) shows the axial load F_a and corresponding peak probe force $F_p^{\max}$ along with the quadratic curve fitting (polynomial fit of order 2). The predicted capacity of the cylinder F_{pre} is 2185.5 N, which is the value of Y axis, where the quadratic curve intercepts it in Fig. 3(*b*). The numerically obtained capacity of the cylinder F_{num}, obtained by finite element analysis of the cylinder, is 2183.0 N that is only 0.11% less than F_{pre}. Again, the proposed procedure is accurately predicting the capacity of the imperfect cylinder with imperfection amplitude $\delta = 0.1t$.

The prediction procedure is also implemented on imperfect cylinders with higher imperfection amplitude. In Fig. 4, the predicted capacities and the actual capacities of imperfect cylinders are shown against the amplitude of the imperfections. Note that the procedure is predicting the capacity of the imperfect cylinders accurately for higher imperfection amplitudes ($0 < \delta \leq 2t$). We again emphasize that in all these computations, the probing is done in the middle of the dimple. This location is not known prior for real structures. The importance and implications of this location will be discussed in Sec. 6 along with the effect of the probing location, and the robustness of the procedure, but before that, we present the experimental implementation of the procedure on mini Coke cans.

4 Experiments on Cylindrical Shells

Our custom-made bi-axial mechanical tester is similar to that detailed in the study by Virot et al. [34] and shown schematically in Fig. 5(*a*). It is designed to study the stability and strength of commercial cylindrical shells (aluminum Coke cans, 7.5 fl oz). A vertical actuator, equipped with a load cell (Futek LCB200), applies an axial load F_a to the inputted sample. Test samples are placed upright between two platens, which can be rotated, even under axial load. To the side, a horizontal linear actuator, also equipped with a load-

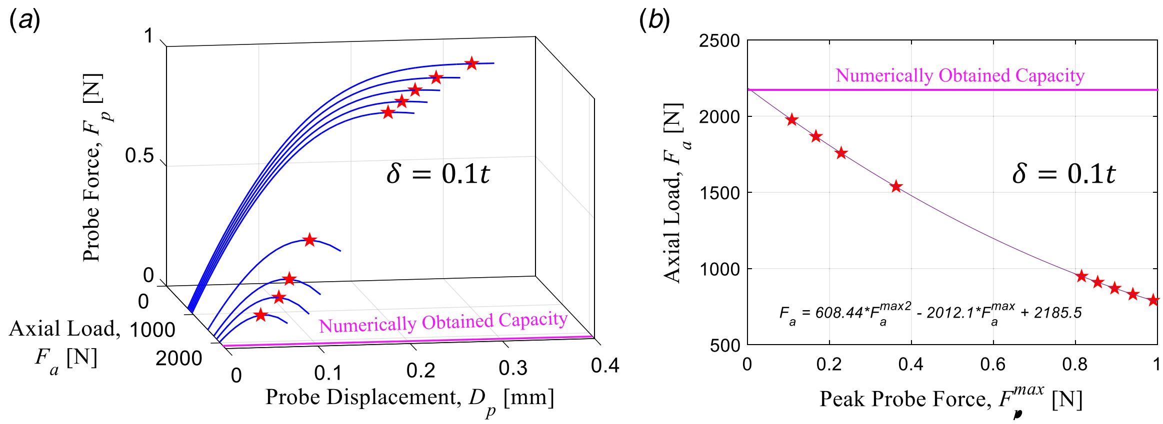

Fig. 3 **(*a*) Stability landscape, which is obtained by implementing the proposed procedure numerically, shown in the three-dimensional phase space of axial load F_a, probe displacement D_p, and probe force F_p. (*b*) The axial load F_a versus peak probe force F_p^{max} data along with its quadratic regression curve. The predicted capacity F_{pre}, where the quadratic curve intercepts *Y* axis, of the cylinder is 2185.5 N, whereas the numerically obtained capacity of the cylinder F_{num} is 2183.0 N and is shown by the horizontal line.**

cell (Futek LSB200), serves as the poker probe. An aluminum marble of diameter 4.75 mm is rigidly attached to the probe's tip and can be raised or lowered vertically along the surface of the shell. Thus, the entire surface of the shell is accessible to the probe. For probing, vertical and horizontal loading are displacement controlled, and horizontal poking is performed under a constant vertical displacement; the axial load is stable to within 2% during poking. Data acquisition and motor controls are accomplished through a custom MATLAB program.

Mini aluminum Coke cans (7.5 fl oz) are used as test samples. These are cylindrical shells of radius $R = 28.6$ mm, thickness $t = 104 \pm 4$ μm (radius-to-thickness ratio $R/t = 274$), and height $L = 107$ mm [36]. A Coke can contains many inherent geometrical imperfections of varying shapes and size, likely from the commercial manufacturing and shipping process [35]. Hence, this system differs from those previously studied by having uncontrolled background imperfections [23–26]. To introduce a controlled geometrical imperfection on the surface of a can, a custom "dimple-maker" is used. The setup consists of an aluminum marble of diameter 3.15 mm with a load-cell (Futek LSB200), which is attached to a vertical linear actuator (Fig. 5(*b*)).

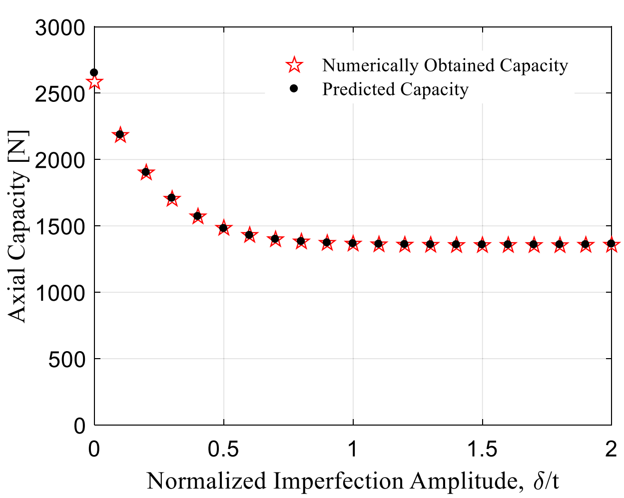

Fig. 4 **Numerically obtained capacity F_{num} (stars) and predicted capacity F_{pre} (circles) of the cylinders. F_{num} is calculated by the finite element analysis, while F_{pre} is found by implementing the proposed procedure. The predictions are accurate as the differences between F_{num} and F_{pre} are very small for all the imperfect cylinders that are considered ($\delta \leq 2t$).**

The force on the indenting aluminum marble F_I increases monotonically as it is pushed into the can's surface, as shown for a typical example in Fig. 6 (Inset). The indenter is advanced to a maximum displacement Δ and then retracted. As the indenter is removed, the force decreases monotonically and a hysteresis is observed in the force–displacement curve. We define the displacement at which the F_I zeros and the indenter detaches as the depth of the imparted dimple δ. The dimple's depth depends on the maximum indenter displacement (Δ), thus allowing a systematic introduction of geometrical imperfections of a set scale, as shown in Fig. 6. Although only the dimple's depth, rather than the precise shape, is measured, their geometric profile is likely similar to those recently computationally explored by Gerasimidis and Hutchinson [22]. As a final note, it is critical that all dimpling be done on unopened, pressurized Coke cans to confine plastic deformations to a small localized region around the marble. Once a dimple is made, the can is depressurized and emptied of its internal contents. Figure 6 indicates that

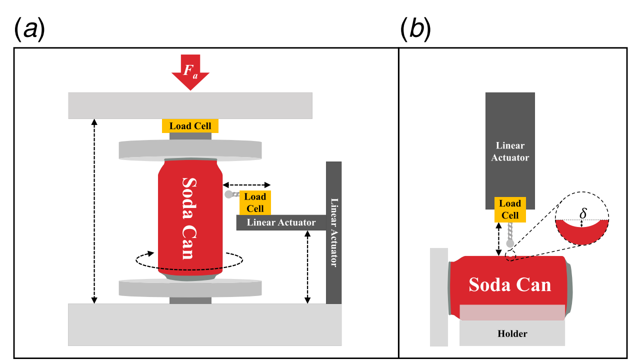

Fig. 5 **(*a*) Diagram of the experimental setup. An empty soda can is placed between the two platens. The platens apply onto the can an axial load F_a, whose magnitude is measured via an attached load cell. Once an axial load is applied, a 4.75 mm ball attached to a load-cell and linear actuator acts as a lateral probe, measuring forces (F_p), and displacements (D_p) while probing from the side. The probe can be moved vertically to any arbitrary height, and the shell can be rotated to any arbitrary angle. (*b*) Diagram of the experimental setup for the imparting of imperfections. A 3.15 mm ball is pushed into an unopened pressurized Coke can to create a permanent indentation along the surface with a specified depth (δ). By measuring the force (F_I) and displacement (D_I) of the indenter as it is pushed into an unopened, pressurised can we can place nearly identical imperfectionsacross many different cans.**

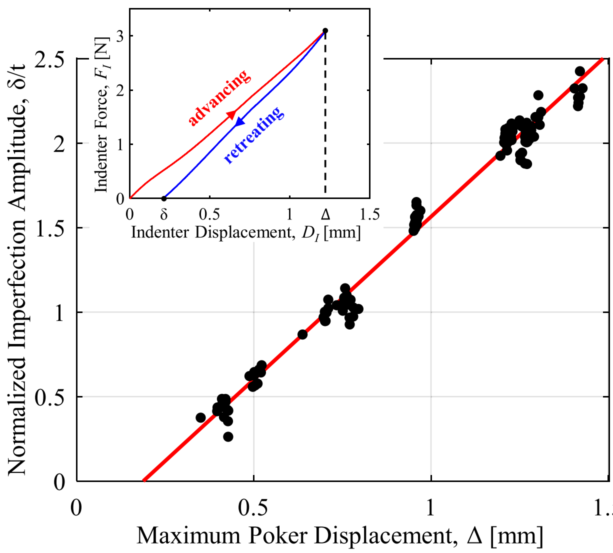

Fig. 6 Prescribed imperfection amplitude (δ), normalized by the can's thickness (t), versus the maximum displacement the indenter was pushed into the unopened, pressurized can's surface (Δ). *Inset* shows a typical example of a force–displacement curve during indentation of a can whose final imperfection is $\delta \approx 2t$. Note that the indenter is pushed into (red) and removed from (blue) the surface of an unopened, pressurized can (Fig. 5(*b*)). (Color version online.)

indentation below $\Delta < 0.2$ mm is entirely elastic, as opposed to that of depressurized cans, which exhibit elastic deformation for indentation displacements on the order of ≈ 1 mm [34]. Repeatedly probing a depressurized shell hundreds of times does not appear to change the axial capacity of the shell or the topography of the stability landscape's ridge. However, further experiments—perhaps using direct imaging of the can's surface—are required to precisely determine what plastic damage might be caused by repeated small indentation probing.

Introducing a dimple provides a well-defined location to probe. As such, the probe pokes at the center of the dimple to extrapolate the can's maximum axial capacity. Specifically, a simple ridge-tracking protocol is implemented, measuring the peak probe force ($F_p^{\max}$) at various axial loads (F_a) and extrapolating to $F_p^{\max} = 0$ to identify the catastrophic axial load (Fig. 7(*b*)) [36]. The ridge-tracking procedure used is similar to that detailed in Sec. 2. In the simulations, a quadratic function was fit to the numerical data and extrapolated to generate a prediction for the failure load; however, in the experiments, small measurement errors extrapolated by a quadratic fit may result in large fluctuations in the early-point prediction. When calculating the next axial load at which to probe, a conservative approach is beneficial to avoid accidentally overloading the can. As such, a linear fit using the last five measured loads, which proved more robust to experimental noise, was used, as shown in Fig. 7.

For larger dimples, whose depth are $\delta \geq 1.5t$, predictions predominantly work to within 0.5% of the actual failure load. For cans with smaller geometrical imperfections, our protocol consistently overpredicts the strength of the sample. The mean axial capacity for cans with a larger dimple ($\delta > 1.25t$) is 1008 *N*, whereas cans with a smaller dimple ($\delta < 1.25t$) have an average capacity of 1210 *N*, which is consistent with the numerical simulations (Fig. 8). Although a larger sized dimple decreases the average strength of our shells, the distribution of loads appears to remain similarly broad. Dimples with nearly identical depths still exhibit a wide range of failure loads, suggesting that the imparted dimple combined with the existing background defects of the system determine the can's strength. In contrast to system's where a single defect dominates [23–26].

5 Application of the Procedure on the Imperfect Cylindrical Shells Having Background Imperfections

In the experiment, with higher imperfection amplitudes ($\delta \geq 1.5t$), the proposed procedure predicts the capacity accurately when probing is done in the middle of the dimple. However, the procedure always overpredicts the capacity when the created dimple has a small amplitude ($\delta \leq 1.5t$). This overprediction is due to the presence of background imperfections, which are not created artificially but were already in the Coke cans. Consequently, for the small amplitude dimple, the prediction overestimates the capacity, whereas for the high amplitude dimple, the prediction is accurate.

To explore the phenomenon of dominating imperfection further, we simulate the can having two dimples, as shown in Fig. 9. The amplitudes are of the order of the thickness of the cylinder. Figure 10(*a*) shows the actual capacities, found by FEA analysis, of this can with varying background and dimple imperfections. Note that the capacity of the can depends on the imperfection that has higher amplitude. For example, when the background is zero,

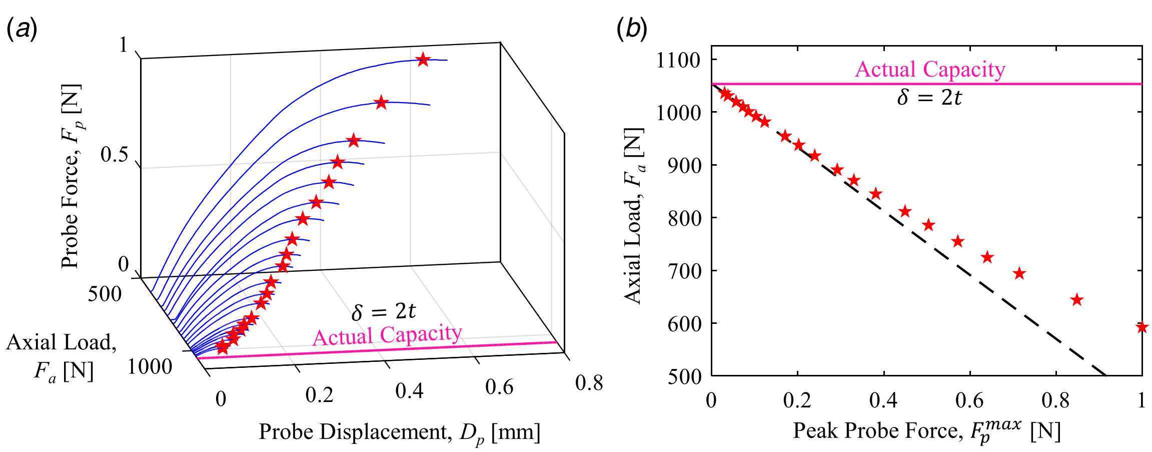

Fig. 7 (*a*) Experimentally obtained stability landscape constructed using the measured axial loads F_a, probe displacements D_p, and probe forces F_p. This specific can has an imperfection amplitude $\delta = 2.081t$. (*b*) The axial loads F_a versus corresponding peak probe forces $F_p^{\max}$, and a linear extrapolation between these two parameters. The predicted capacity, where the linear curve intercepts the *y*-axis is 1054.6 N, whereas the actual capacity of the soda can is 1053.1 N. Hence, the error for this prediction is 0.14%.

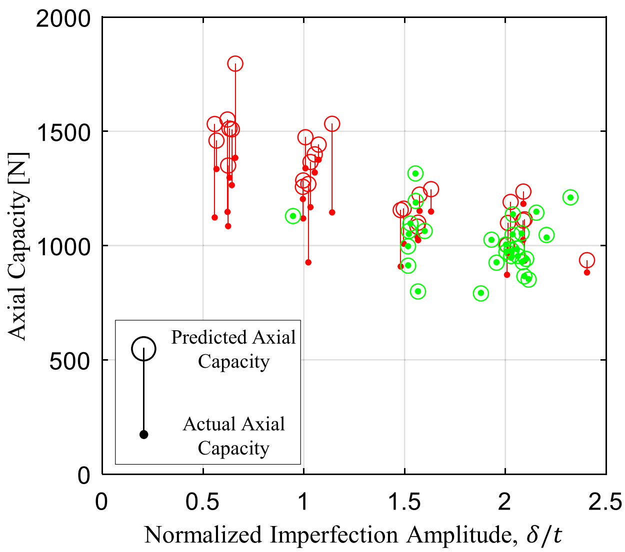

Fig. 8 Experimental predictions for different imperfection amplitudes. Each datum represents an individual can for which the axial capacity was predicted, via ridge tracking (see Fig. 7). The data have been separated by the amplitudes of the imperfections imparted onto each individual coke can. Failed predictions consistently occur for small amplitudes ($\delta < 1.25t$), indicating that a minimum threshold exists for an imperfection to dominate over existing background defects. Successful predictions, overwhelming occur with larger amplitude imperfections ($\delta > 1.25t$). However, some large imperfections can lead to an unsuccessful prediction, emphasizing the importance that background defects have on a shell's load bearing capacity.

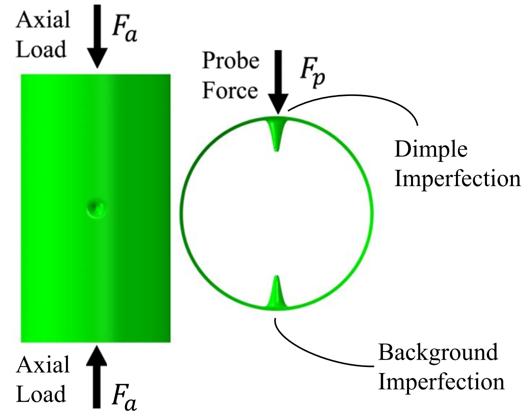

Fig. 9 Rendering of the model can with two dimple imperfections along with axial load (F_a) and probe force (F_p). The dimples are modeled as a two-dimensional normal distribution density function whose value is exponentially small well away from the dimple center [18,50]. The dimples are located in the middle section of the cylinder and dramatically opposite direction. We refer to the first dimple as the dimple imperfection and to the second dimple as background imperfection. The probing is done in the center of the dimple imperfection. The amplitude of the dimples is scaled up so the dimples are visible; in our analyses, the amplitudes are of the order of the thickness of the can.

the capacity depends on the dimple imperfection amplitude (X-axis) as the capacity is reduced with an increase in the dimple imperfection amplitude. For the background imperfection $0.2t$, the curve is flat till the dimple imperfection amplitude is less than $0.2t$, indicating that the capacity is decided by the background imperfection. Similarly, for the background imperfection $0.5t$, the curve is flat until the background imperfection is less than $0.5t$. Furthermore, for the background imperfection $2.0t$, the curve is always flat, and the variation of dimple imperfection amplitude does not affect the capacity as it is, always, less than $2.0t$. It is clear from this analysis that the capacity of cylinders is decided by the imperfection that has the highest imperfection amplitude. Here, we use a simple model for the background imperfection; in reality, background imperfections are complex. Nevertheless, this simple model explains the concept of dominating imperfection.

Figure 10(*b*) shows the predicted capacity of the can; the predicted capacities are almost the same for all the cases irrespective to the background imperfection and follow the actual capacity of the can without the background imperfection of Fig. 10(*a*). The probing can only gauge the imperfections that are near to the point of probing. Thus, the predicted capacity is accurate only if there is no other dominating imperfection away from the point of probing. The predicted capacity of Fig. 10(*b*) is accurate if the background imperfection amplitude is less than the dimple imperfection amplitude. Otherwise, the prediction overestimates the capacity. For example, when the background imperfection is $0.2t$ and dimple imperfection is $0.5t$, the predicted capacity (Fig. 10(*b*)) and actual capacity (Fig. 10(*a*)) are the same. But, when the

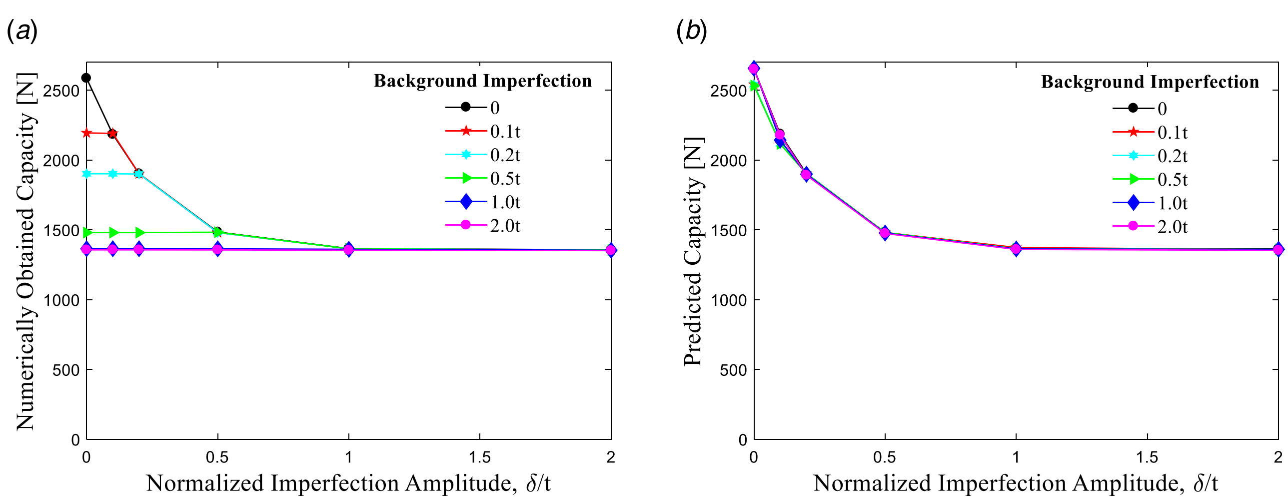

Fig. 10 (*a*) Numerically obtained capacity F_{num} of the can with background imperfection as a function of the amplitude of dimple imperfection that varies from 0 to 2:0t. (*b*) Predicted capacities F_{pre} of the can with background imperfection. For the prediction, probing is done in the middle of the dimple. The predicted capacity of F_{pre} is accurate if the background imperfection amplitude is less than the dimple imperfection amplitude. Otherwise, the prediction overestimates the capacity.

background imperfection is $0.5t$ and dimple imperfection is $0.2t$, the predicted capacity (Fig. 10(*b*)) is more than the actual capacity (Fig. 10(*a*)). The same pattern is observed for all the cases. This simulation is consistent with the experimental results showing that the prediction is accurate when the created dimple has a high amplitude. For these cases, it is more probable that the dimple imperfection will be the dominating one. As a result, the chances of an accurate prediction increase, as also observed in the experiments. This observation reflects the crucial role played by the location of probing. To further investigate this issue, we move the location of the probing away from the imperfection in the axial and circumferential directions. The results are presented in Sec. 6.

6 Effect of the Location of Probing Relative to the Imperfections

In Sec. 5, it has been demonstrated that the prediction of the buckling capacity of thin cylinders is accurate if the probing is done at the dominating imperfection. In this section, we further explore the issue of the probing location, both computationally and experimentally, by moving the probing location away from the imperfection in the axial and in the circumferential directions.

6.1 Computational Study. We create a dimple-like imperfect cylinder similar to the one described in Sec. 3 and shown in Fig. 2. First, we implement the proposed procedure of Sec. 2, but we probe away from the middle of the dimple. We showed in Sec. 3 how probing in the center of the dimple can provide accurate predictions of failure for the cylinder. Here, we will show that probing around the dominant imperfection (the imperfection that dictates the capacity of thin cylinders) consistently introduces a length scale at which probing proves ineffective. Having asserted that now we address a more fundamental question: Is it possible to predict the capacity of thin cylinders by probing away from the dominant imperfection? To answer this question, the axially loaded imperfect cylinder is probed away from the imperfection, and probing data are used to predict the capacity.

Figure 11 shows the plots of axial load F_a against the peak probe force $F_p^{\max}$ when the probing is done away from the middle of the imperfection along the circumferential direction, for imperfection amplitudes $\delta = 1.0t$ (Fig. 11(*a*)) and $2.0t$ (Fig. 11(*b*)). We chose seven locations along the circumferential direction, i.e., $\theta = 0$ deg, 3.7 deg, 10 deg, 30 deg, 45 deg, 90 deg, 135 deg, and 180 deg, where θ is the angular distant between the probing location and the middle of the imperfection. $\theta = 0$ deg represents probing, which is done in the middle of the imperfection that yields accurate prediction. Figure 11 also shows the plot for the perfect cylinder.

For $\delta = 1.0t$, the curves for 30 deg, 45 deg, 90 deg, 135 deg, and 180 deg follow the curve of the perfect cylinder; and the probing fails to recognize the presence of the imperfection. Consequently, they predict the capacity of a perfect cylinder instead of the actual cylinder. These results indicate that the probing fails to recognize the presence of imperfection if it is done away from the region of influence of the imperfection. Here, we use the term "region of influence" to describe a region near the imperfection such that if the probing is done outside this region, the presence of the imperfection is undetectable. For example, 30 deg, 45 deg, 90 deg, 135 deg, and 180 deg are outside from the region of influence in Fig. 11(*a*). While for $\theta = 3.7$ deg and $\theta = 10$ deg, the F_a and $F_p^{\max}$ plots match, although not exactly, the plot of the imperfect cylinder with $\theta = 0$ deg. This means that when $\theta = 3.7$ deg or $\theta = 10$ deg, the probing location lies in the region of influence of the imperfection, and thus, the predicted value is near the exact value of the imperfect cylinder. It should be noted that when the probing is in the region of influence, this does not necessarily indicates that the prediction will be accurate; instead, it only means that the imperfection has some influence on the F_a and $F_p^{\max}$ plot. For imperfection amplitude $\delta = 2.0t$, a similar pattern is emerged as shown in Fig. 11(*b*).

Figure 12 shows the axial load F_a against the peak probe force $F_p^{\max}$ when the probing is done away from the middle of the imperfection along the axial direction, for the imperfection amplitude $\delta = 1.0t$ and $2.0t$. We chose five locations along the axial direction, i.e., $x = 0$, 2λ, 4λ, 6λ, and 8λ, where x is the distance between the probing location and the middle of dimple, and λ is the classical axisymmetric buckle half-wavelength for cylindrical shells under axial load, as given in Eq. (6). $x = 0$ represents probing that is done in the middle of the imperfection, which yields accurate prediction. Figure 12 also shows the plot for the perfect cylinder.

For the four cases, $x = 2\lambda$, 4λ, 6λ, and 8λ, probing behavior can be divided in two distinctive regions depending on the axial load F_a. The first region is when the probing is unable to detect the imperfection for small axial loads F_a, we call it region 1. For region 1, F_a and $F_p^{\max}$ curves of $x = 2\lambda$, 4λ, 6λ, and 8λ follow the curve of the perfect cylinder as shown in Fig. 12. The second region is when the imperfection influence the probing behavior for axial loads F_a close to cylinder's capacity, we call it region 2. For region 2, F_a and $F_p^{\max}$ curves of $x = 2\lambda$, 4λ, 6λ, and 8λ bent

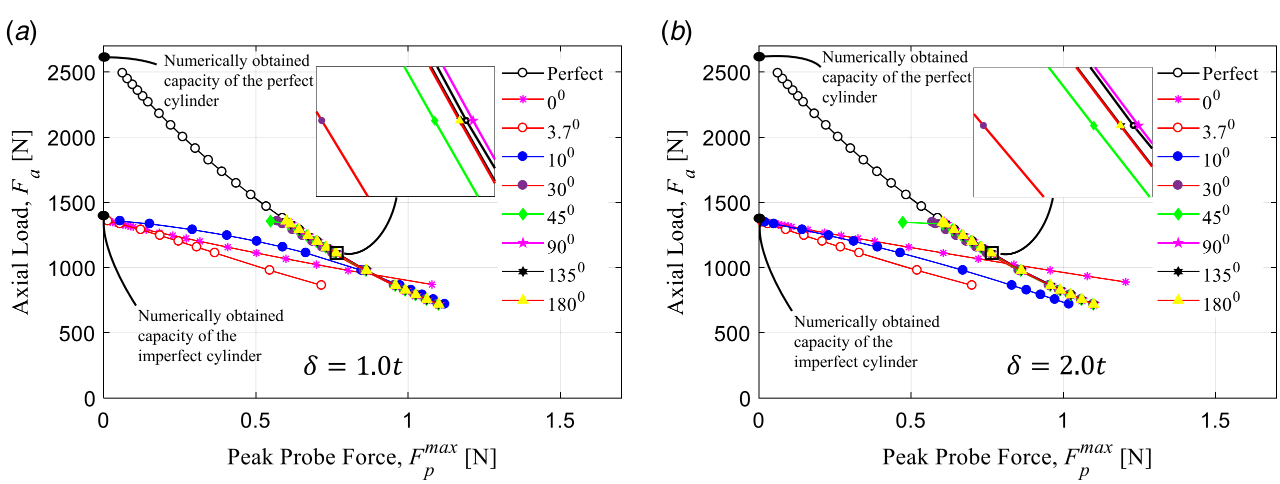

Fig. 11 Numerically obtained axial load F_a versus peak probe force $F_p^{\max}$ for the probing locations at $\theta = 0$ deg, 3.7 deg, 10 deg, 30 deg, 45 deg, 90 deg, 135 deg, and 180 deg relative to the middle of imperfection along the circumferential direction, for imperfection amplitudes (*a*) $\delta = 1.0t$ and (*b*) $\delta = 2.0t$. The curves shown are not algorithmic fits but rather lines drawn between each point, solely for visualization purposes. The curve for the perfect cylinder is also shown. The imperfection has no influence on the probing for $\theta = 30$ deg, $\theta = 45$ deg, 90 deg, 135 deg, and 180 deg, and thus, the predictions are inaccurate.

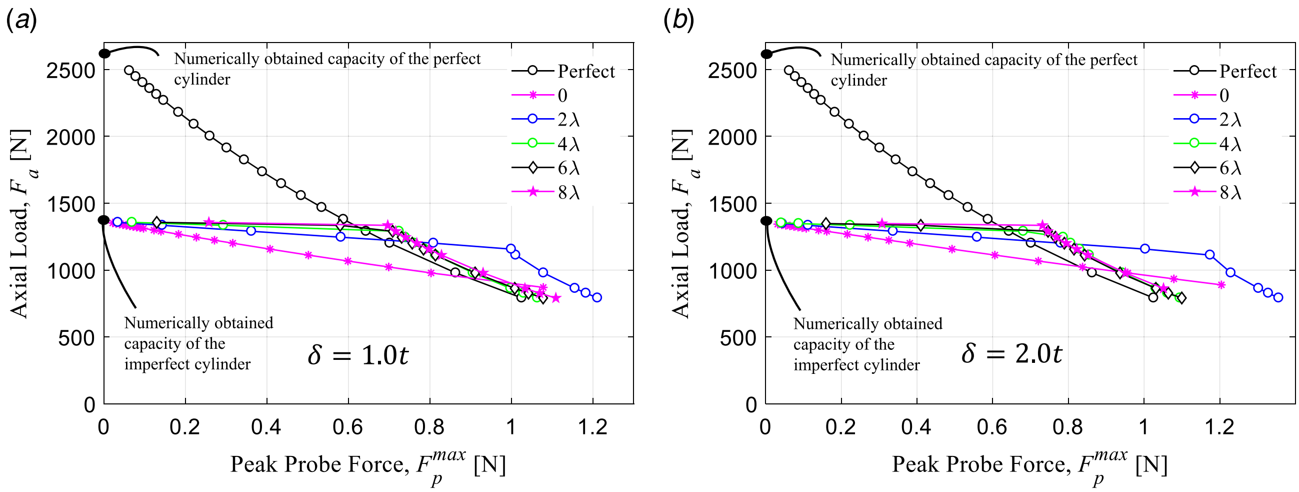

Fig. 12 Numerically obtained axial load F_a versus peak probe force F_p^{max} for the probing locations at $x = 0$, 2λ, 4λ, 6λ, and 8λ relative to the middle of imperfection along the axial direction, for imperfection amplitudes (a) $\delta = 1.0t$ and (b) $\delta = 2.0t$. The curves shown are not algorithmic fits but rather lines drawn between each point, solely for visualization purposes. The curve for the perfect cylinder is also shown. The imperfection has no influence on the probing for $x = 2\lambda$, 4λ, 6λ, and 8λ, and thus, the predictions are inaccurate.

sharply as shown in Fig. 12, and capacity can be predicted. Practically, this sharp bend happens close to the cylinder's capacity, which makes the cylinder under the axial load F_a unstable.

Figure 13 shows the three-dimensional phase space of axial load F_a, probe displacement D_p, and probe force F_p corresponding to $\delta = 2.0t$ and $x = 4\lambda$. For the last three plots corresponds to higher F_a, the probe returns before reaching the peak; this is a kind of instability. We cannot probe the cylinder under axial load that is near to the capacity of the imperfect cylinder. It also explains the reason behind the bending of the F_a and $F_p^{\max}$ plots in region 2; this bending is happening because the $F_p^{\max}$ is not the peak probe force but the maximum probe force that can be achieved by probing at the higher F_a. As a result, the data in region 2 cannot be used for the prediction.

From these analyses, it is clear that the probing location relative to the imperfection is crucial information, and the prediction would be inaccurate if the probing is away from the imperfection. These analyses also reveal some interesting phenomena: (1) there exists a region of influence of the imperfection, and if probing is in this region, the imperfection affects the probing profile, otherwise, the probing profile is the same as for the perfect cylinder. The area of this region of influence depends on the imperfection amplitude and shape. (2) If the probing is done near the axial capacity of the cylinders, the probing might cause the failure of the cylinders. Thus, some safety margin between the axial load and the capacity must be maintained. Our experiments also support these results, which are described in Sec. 6.2.

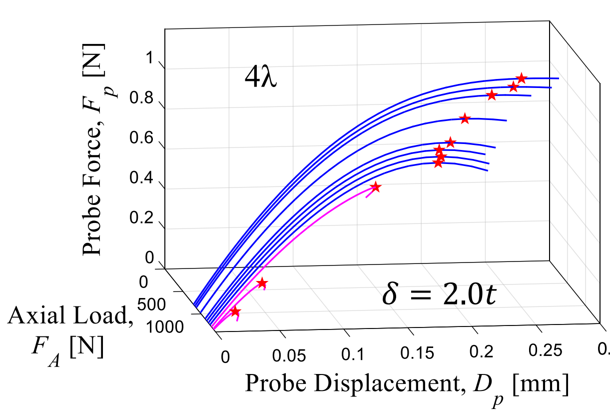

Fig. 13 Numerically obtained stability landscape. A three-dimensional phase space of axial load F_a, probe displacement D_p, and probe force F_p corresponds to $\delta = 2.0t$, and $x = 4\lambda$. For the three curves corresponding to higher axial loads F_a, the probe returns before reaching the peak. This is a kind of instability, and thus, we cannot probe cylinders under axial loads that are near to the capacity of the cylinders.

6.2 Experimental Study. Simulations reveal the existence of a "region of influence" in which the stability landscape is modified by the presence of the dimple. Analogous to the simulations, we experimentally probe the vicinity of the dimple imperfection, generating landscapes at various locations. Initially, the center of the dimple is probed before moving to other predetermined locations

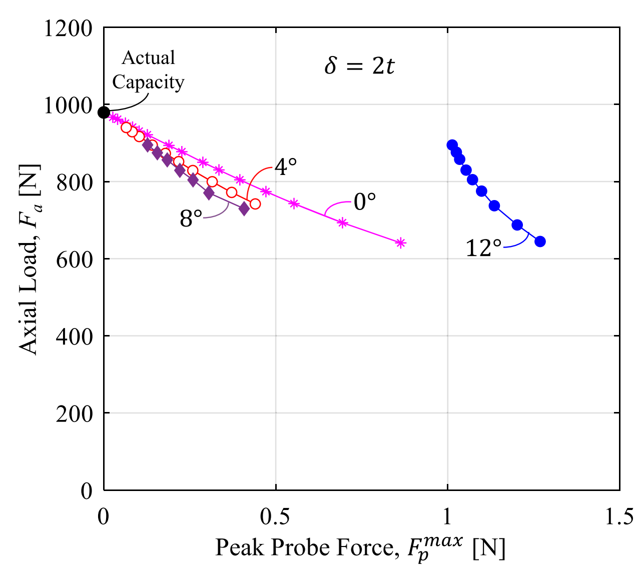

Fig. 14 Experimentally obtained axial loads F_a and corresponding peak probe forces F_p^{max} for the probing locations at $\theta = 0$ deg, 4 deg, 8 deg, and 12 deg relative to the middle of imperfection along the circumferential direction, for imperfection amplitude $\delta = 2t$. The curves shown are not algorithmic fits but rather lines drawn between each point, solely for visualization purposes. The probing fails to recognize the presence of the imperfection for $\theta \gtrapprox 8$ deg and thus reverts to the prediction of a perfect shell.

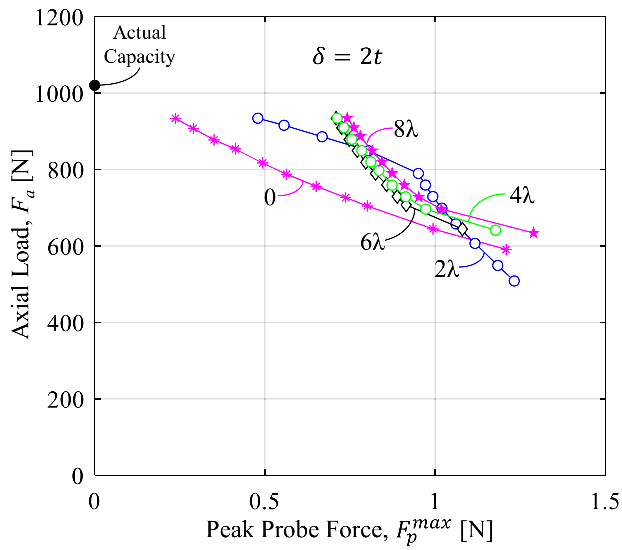

Fig. 15 Experimentally obtained axial loads F_a and corresponding peak probe forces F_p^{max} from probing at $x = 0$, 2λ, 4λ, 6λ, and 8λ relative to the middle of imperfection along the axial direction, for imperfection amplitude $\delta = 2t$. The curves shown are not algorithmic fits but rather lines drawn between each point, solely for visualization purposes. The probing fails to recognize the presence of the imperfection for $x \gtrapprox 2\lambda$ and thus reverts to the prediction of a perfect shell.

axially and circumferentially. At locations near the boundary of the region of influence, the axial loads are restricted to prevent probe-induced catastrophic buckling. Overall, the experimental observations are consistent with those obtained via finite element simulations, showing qualitatively identical behavior.

The experimental results show a region in both the circumferential (Fig. 14) and axial directions (Fig. 15) extending several centimeters from the center of the dimple. Axially, the size of this region is a function of the applied axial load. For example, at 2λ, there is a discontinuity in the slope of the peak probe loads at ≈800 N. For loads higher than 800 N, the region of influence expands to include the probing location, leading to an accurate capacity prediction. Simulations show similar inflections, even for the furthest of axial locations (Fig. 12), but only at loads extraordinarily close to

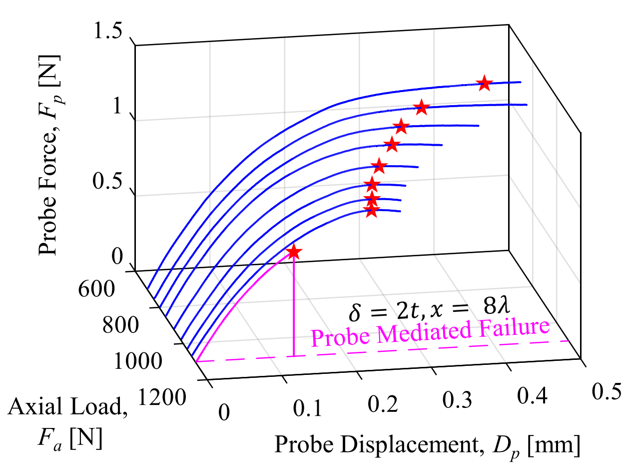

Fig. 16 Experimentally obtained stability landscape generated for a $\delta = 2t$ dimple at $x = 8\lambda$. Probing at the center of the dimple provided a predicted capacity of 1163.8 *N*. However, at a axial height of 8λ, a probe-mediated buckling occurs at 1101.0 *N*, expressed as a sudden drop in F_p. This behavior can be observed when probing at axial distances greater than 3λ.

shell's capacity. Notably, the slope of the peak probe forces always appears continuous in our circumferential data (Fig. 14). In other words, these experiments do not exhibit a growth in the region of influence for the circumferential direction, but further experiments are necessary to confirm this.

As the axial load increases, the region of influence expands axially, and a new instability is experimentally observed. At axial locations far from the dimple ($x > 2\lambda$), a probe-mediated buckling event may destroy the sample (Fig. 16). This failure is violent, sudden, and catastrophic, occurring before the expected peak probe force, based on previous points along the landscape's ridge, and often 5–10% below the shell's predicted capacity. Following such poker-mediated failure, the surface of the shell consistently exhibits a diamond-shaped buckle centered at the dimple. These discontinuities have also been observed when probing undimpled, normal Coke cans at high loads (>900 N) [34–36].

7 Conclusions

We have proposed a nondestructive procedure to predict the buckling capacity of thin cylindrical shells. This procedure is implemented computationally on cylindrical shells and experimentally on mini Coke cans. For a perfect shell, computational implementation of the procedure predicts accurate results. The percentage difference between the predicted capacity F_{pre} and numerically obtained capacity F_{num} is 2.5% ($|F_{num} - F_{pre}|/F_{num} \times 100$); this shows that the proposed procedure is predicting the capacity of a perfect cylinder accurately. For the imperfect can, the computational implementation yields accurate results when the probing is done in the middle of the imperfection. The percentage difference between the F_{pre} and F_{num} is 0.11% for imperfection amplitude $\delta = 0.1t$. For other imperfection amplitudes we also had very accurate predictions. However, the procedure overpredicts the capacity of the cans when the probing is done away from the imperfection; the probing fails to recognize the presence of imperfection and the predicted capacity is near to the capacity of the perfect can instead of imperfect one. This demonstrates the crucial role of probing location. Another significant finding is the phenomenon of dominating imperfection: if more than one imperfection is present in the cylinder, the capacity is dictated by the dominating imperfection.

Similar predictive success is achieved in the experimental results. By imparting a dimple onto a commercial Coke can, whose preexisting defects are unknown, one can extract a stability landscape by probing at or within the near vicinity of the dimple. For dimple's with imperfection amplitudes $\geq 1.5t$, the features of the stability landscape can be extrapolated to accurately characterize the failure properties of the shell. Probing around a dimple reveals stable and unstable regions. In the stable regions, the ridge of the landscape varies based on location, but remains capable of predicting the shell's failure properties. In the unstable regions, the probe can induce catastrophic failure in the shell.

Both computational and experimental results suggest that the prediction of the strength of imperfect cylinders is possible if the probing is done at the proper location. Although finding the proper probing location in a real cylinder is a challenge. Nevertheless, this study gives hope that a framework can be developed for nondestructive experiments to predict the buckling capacity of thin shells.

Acknowledgment

This work was supported by the National Science Foundation (DMR-1420570). S. M. R. and N. L. C. acknowledge support from the Google Faculty Research Awards (2019). S. M. R. acknowledges support from the Alfred P. Sloan Research Foundation (FG-2016-6925). This work also benefited from the contributions of Lewis R. B. Picard, Nathaniel B. Vilas, and Jonathan Zauberman, who helped carry the experimental setup up several flights of stairs.

Conflict of Interest

There are no conflicts of interest.

Data Availability Statement

The datasets generated and supporting the findings of this article are obtainable from the corresponding author upon reasonable request. The authors attest that all data for this study are included in the paper. Data provided by a third party listed in Acknowledgment.

References

[1] Tsien, H.-S., 1942, "A Theory for the Buckling of Thin Shells," J. Aeronautical Sci., **9**(10), pp. 373–384.

[2] von Karman, T., 1941, "The Buckling of Thin Cylindrical Shells Under Axial Compression," J. Aeronautical Sci., **8**(8), pp. 303–312.

[3] von Karman, T., and Tsien, H.-S., 1939, "The Buckling of Spherical Shells by External Pressure," J. Aeronautical Sci., **7**(2), pp. 43–50.

[4] Koiter, W. T., 1945, "The Stability of Elastic Equilibrium," Ph.D. thesis, Deft University of Technology, Delft, The Netherlands. An English Translation is Available in 1967.

[5] Hutchinson, J., and Koiter, W., 1970, "Postbuckling Theory," ASME Appl. Mech. Rev., **23**(12), pp. 1353–1366.

[6] Brush, D. O., and Almroth, B. O., 1975, *Buckling of Bars, Plates, and Shells*, Vol. 6, McGraw-Hill, New York.

[7] Elishakoff, I., 2012, "Probabilistic Resolution of the Twentieth Century Conundrum in Elastic Stability," Thin-Walled Struct., **59**, pp. 35–57.

[8] Wagner, H., Hühne, C., Niemann, S., and Khakimova, R., 2017, "Robust Design Criterion for Axially Loaded Cylindrical Shells—Simulation and Validation," Thin-Walled Struct., **115**, pp. 154–162.

[9] Wagner, H., Hühne, C., and Niemann, S., 2018, "Robust Knockdown Factors for the Design of Spherical Shells Under External Pressure: Development and Validation," Int. J. Mech. Sci., **141**, pp. 58–77.

[10] Evkin, A. Y., and Lykhachova, O. V., 2019, "Design Buckling Pressure for Thin Spherical Shells: Development and Validation," Int. J. Solids. Struct., **156**, pp. 61–72.

[11] Reis, P. M., 2015, "A Perspective on the Revival of Structural (in) Stability With Novel Opportunities for Function: From Buckliphobia to Buckliphilia," ASME J. Appl. Mech., **82**(11), p. 111001.

[12] Holmes, D. P., Lee, J.-H., Park, H. S., and Pezzulla, M., 2020, "Nonlinear Buckling Behavior of a Complete Spherical Shell Under Uniform External Pressure and Homogenous Natural Curvature," Phys. Rev. E, **102**(2), p. 023003.

[13] Thompson, J., 1962, "The Elastic Instability of a Complete Spherical Shell," Aeronautical Q., **13**(2), pp. 189–201.

[14] Hutchinson, J. W., 1967, "Imperfection Sensitivity of Externally Pressurized Spherical Shells," ASME J. Appl. Mech., **34**(1), pp. 49–55.

[15] Wullschleger, L., 2006, "Numerical Investigation of the Buckling Behaviour of Axially Compressed Circular Cylinders Having Parametric Initial Dimple Imperfections," Ph.D. thesis, ETH Zurich, Zurich, Switzerland.

[16] Champneys, A. R., Dodwell, T. J., Groh, R. M., Hunt, G. W., Neville, R. M., Pirrera, A., Sakhaei, A. H., Schenk, M., and Wadee, M. A., 2019, "Happy Catastrophe: Recent Progress in Analysis and Exploitation of Elastic Instability," Frontiers Appl. Math. Stat., **5**, p. 201900034.

[17] Hutchinson, J. W., 2020, "Eml Webinar Overview: New Developments in Shell Stability," Extreme Mech. Lett., **39**, p. 100805.

[18] Yadav, K. K., and Gerasimidis, S., 2019, "Instability of Thin Steel Cylindrical Shells Under Bending," Thin-Walled Struct., **137**, pp. 151–166.

[19] Yadav, K. K., and Gerasimidis, S., 2020, "Imperfection Insensitive Thin Cylindrical Shells for Next Generation Wind Turbine Towers," J. Constr. Steel. Res., **172**, p. 106228.

[20] Weingarten, V. I., Seide, P., and Peterson, J., 1968, "Buckling of Thin-Walled Circular Cylinders," NASA SP-8007.

[21] European Standard EN 1993-1-6, 2007, "Design of Steel Structures Part-1–6: Strength and Stability of Shell Structures," CEN (European Committee for Standardization), Brussels, Belgium, Technical Report.

[22] Gerasimidis, S., and Hutchinson, J., 2020, "Dent Imperfections in Shell Buckling: The Role of Geometry, Residual Stress and Plasticity," J. Appl. Mech., **10**, pp. 1–23.

[23] Lee, A., López Jiménez, F., Marthelot, J., Hutchinson, J. W., and Reis, P. M., 2016, "The Geometric Role of Precisely Engineered Imperfections on the Critical Buckling Load of Spherical Elastic Shells," ASME J. Appl. Mech., **83**(11), p. 111005.

[24] Jiménez, F. L., Marthelot, J., Lee, A., Hutchinson, J. W., and Reis, P. M., 2017, "Technical Brief: Knockdown Factor for the Buckling of Spherical Shells Containing Large-Amplitude Geometric Defects," ASME J. Appl. Mech., **84**(3), p. 034501.

[25] Marthelot, J., López Jiménez, F., Lee, A., Hutchinson, J. W., and Reis, P. M., 2017, "Buckling of a Pressurized Hemispherical Shell Subjected to a Probing Force," ASME J. Appl. Mech., **84**(12), p. 121005.

[26] Yan, D., Pezzulla, M., and Reis, P. M., 2020, "Buckling of Pressurized Spherical Shells Containing a Through-Thickness Defect," J. Mech. Phys. Solids., **138**, p. 103923.

[27] Katifori, E., Alben, S., Cerda, E., Nelson, D. R., and Dumais, J., 2010, "Foldable Structures and the Natural Design of Pollen Grains," Proc. Natl. Acad. Sci. USA, **107**(17), pp. 7635–7639.

[28] Dinsmore, A., Hsu, M. F., Nikolaides, M., Marquez, M., Bausch, A., and Weitz, D., 2002, "Colloidosomes: Selectively Permeable Capsules Composed of Colloidal Particles," Science, **298**(5595), pp. 1006–1009.

[29] Lee, A., Brun, P.-T., Marthelot, J., Balestra, G., Gallaire, F., and Reis, P. M., 2016, "Fabrication of Slender Elastic Shells by the Coating of Curved Surfaces," Nat. Commun., **7**(1), pp. 1–7.

[30] Thompson, J. M. T., 2015, "Advances in Shell Buckling: Theory and Experiments," Int. J. Bifurcat. Chaos, **25**(1), p. 1530001.

[31] Thompson, J. M. T., and Sieber, J., 2016, "Shock-Sensitivity in Shell-Like Structures: With Simulations of Spherical Shell Buckling," Int. J. Bifurcat. Chaos, **26**(2), p. 1630003.

[32] Thompson, J. M. T., Hutchinson, J. W., and Sieber, J., 2017, "Probing Shells Against Buckling: A Nondestructive Technique for Laboratory Testing," Int. J. Bifurcat. Chaos, **27**(14), p. 1730048.

[33] Hutchinson, J. W., and Thompson, J. M. T., 2017, "Nonlinear Buckling Interaction for Spherical Shells Subject to Pressure and Probing Forces," ASME J. Appl. Mech., **84**(6), p. 061001.

[34] Virot, E., Kreilos, T., Schneider, T. M., and Rubinstein, S. M., 2017, "Stability Landscape of Shell Buckling," Phys. Rev. Lett., **119**, p. 224101.

[35] Fan, H., 2019, "Critical Buckling Load Prediction of Axially Compressed Cylindrical Shell Based on Non-Destructive Probing Method," Thin-Walled Struct., **139**, pp. 91–104.

[36] Abramian, A., Virot, E., Lozano, E., Rubinstein, S. M., and Schneider, T. M., 2020, "Nondestructive Prediction of the Buckling Load of Imperfect Shells," Phys. Rev. Lett., **125**, p. 225504.

[37] Hunt, G., Lord, G. J., and Peletier, M. A., 2003, "Cylindrical Shell Buckling: A Characterization of Localization and Periodicity," Discrete Continuous Dyn. Syst.-B, **3**(4), p. 505.

[38] Horák, J., Lord, G. J., and Peletier, M. A., 2006, "Cylinder Buckling: the Mountain Pass as an Organizing Center," SIAM J. Appl. Math., **66**(5), pp. 1793–1824.

[39] Vaziri, A., and Mahadevan, L., 2008, "Localized and Extended Deformations of Elastic Shells," Proc. Natl. Acad. Sci. USA, **105**(23), pp. 7913–7918.

[40] Kreilos, T., and Schneider, T. M., 2017, "Fully Localized Post-Buckling States of Cylindrical Shells Under Axial Compression," Proc. R. Soc. A: Math., Phys. Eng. Sci., **473**(2205), p. 20170177.

[41] Audoly, B., and Hutchinson, J. W., 2020, "Localization in Spherical Shell Buckling," J. Mech. Phys. Solids., **136**, p. 103720.

[42] Hutchinson, J. W., 2016, "Buckling of Spherical Shells Revisited," Proc. R. Soc. A: Math., Phys. Eng. Sci., **472**(2195), p. 20160577.

[43] Hutchinson, J. W., and Thompson, J. M. T., 2017, "Nonlinear Buckling Behaviour of Spherical Shells: Barriers and Symmetry-Breaking Dimples," Philosophical Trans. R. Soc. A: Math., Phys. Eng. Sci., **375**(2093), p. 20160154.

[44] Hutchinson, J. W., and Thompson, J. M. T., 2018, "Imperfections and Energy Barriers in Shell Buckling," Int. J. Solids. Struct., **148**, pp. 157–168.

[45] Baumgarten, L., and Kierfeld, J., 2019, "Shallow Shell Theory of the Buckling Energy Barrier: From the Pogorelov State to Softening and Imperfection Sensitivity Close to the Buckling Pressure," Phys. Rev. E, **99**(2), p. 022803.

[46] Lozano, E., Rubinstein, S., and Schneider, T., 2019, "How Localized Imperfections Modify the Buckling Threshold of Cylindrical Shells," APS, **2019**, pp. X55–002.

[47] Simulia, 2014, *ABAQUS Theory Manual*, Dassault Systems Simulia Corporation, Providence, RI.

[48] Haynie, W., Hilburger, M., Bogge, M., Maspoli, M., and Kriegesmann, B., 2012, "Validation of Lower-Bound Estimates for Compression-Loaded Cylindrical Shells," 53rd AIAA/ASME/ASCE/AHS/ASC Structures, Structural Dynamics and Materials Conference.

[49] Riks, E., 1979, "An Incremental Approach to the Solution of Snapping and Buckling Problems," Int. J. Solids. Struct., **15**(7), pp. 529–551.

[50] Gerasimidis, S., Virot, E., Hutchinson, J., and Rubinstein, S., 2018, "On Establishing Buckling Knockdowns for Imperfection-Sensitive Shell Structures," ASME J. Appl. Mech., **85**(9), pp. 091010.

[51] Timoshenko, S. P., and Gere, J. M., 1961, *Theory of Elastic Stability*, McGraw-Hill, New York.